

Elastic scattering of the $^{12}\text{B} + ^{58}\text{Ni}$ system at near-barrier energies

E. O. N. Zevallos,¹ V. Guimarães,¹ E. N. Cardozo,² J. Lubian,² R. Linares,² R. Lichtenthäler Filho,¹ K. C. C. Pires,¹ O. C. B. Santos,¹ S. Appannababu,¹ E. Crema,¹ J. Alcantara-Núñez,¹ A. L. Lara,¹ Y. S. Villamizar,¹ U. Umbelino,¹ N. Added,¹ M. Assuncao,³ V. Morcelle,⁴ and D. S. Monteiro^{5,6}

¹*Instituto de Física, Universidade de São Paulo, Rua do Matão, 1371, São Paulo 05508-090, São Paulo, Brazil*

²*Instituto de Física, Universidade Federal Fluminense, Avenida Litorânea s/n, Gragoatá, Niterói, 24210-340 Rio de Janeiro, Brazil*

³*Departamento Física, Universidade Federal de São Paulo, Campus Diadema, São Paulo, Brazil*

⁴*Departamento de Física, Universidade Federal Rural do Rio de Janeiro, Seropédica, 23890-000 Rio de Janeiro, Brazil*

⁵*Universidade Federal da Integração Latino-Americana, Instituto Latino-Americano de Ciências da Vida e da Natureza, Foz do Iguaçu, Paraná, Brazil*

⁶*Physics Department, University of Notre Dame, Notre Dame, Indiana, USA*



(Received 27 November 2018; revised manuscript received 16 February 2019; published 19 June 2019)

Elastic scattering of a radioactive neutron-rich boron isotope, ^{12}B , has been measured for the first time. Angular distributions for the elastic scattering of $^{12}\text{B} + ^{58}\text{Ni}$ have been measured at $E_{\text{lab}} = 30.0$ and 33.0 MeV, which are just above the Coulomb barrier ($V_B = 24$ MeV). The obtained angular distributions were analyzed in terms of the large-scale coupled channel (CC) and coupled reaction channel (CRC) calculations, where several inelastic transitions for the target, as well as the most relevant transfer reactions, have been included in the coupling matrix elements. The roles of the spin reorientation and spin-orbit interaction in the reaction mechanism were also investigated. The one-neutron transfer reaction through a coupled reaction calculation had some effect on the elastic scattering of the system studied.

DOI: [10.1103/PhysRevC.99.064613](https://doi.org/10.1103/PhysRevC.99.064613)

I. INTRODUCTION

Elastic scattering measurements induced by light radioactive nuclei have attracted much interest in recent years, in particular at energies close to the barrier, because of the possibility of investigating surface effects and nuclear structure of the projectiles [1,2]. Some light radioactive nuclei, such as ^6He , ^8B , ^{11}Be , and ^{15}C have low separation energy of the valence particle and strong cluster configuration, which can produce a decoupling between the valence particle and the core. The exotic structure of these light nuclei alters the elastic scattering enhancing breakup and/or transfer probabilities. Because of the lower binding energy of the weakly bound light nuclei, the breakup can become an important competing mechanism even at relatively low incident energies, and coupled channel analysis would be required. For light and tightly bound nuclei, other effects such as ground-state deformation, quadrupole excitation, and reorientation can play a role in the elastic process [3–5]. Elastic scattering using boron isotopes as projectiles has been shown to be an interesting case to investigate several effects which can be present in the process. Elastic scattering of radioactive weakly bound and proton-rich ^8B ($J^\pi = 2^+$) projectiles on a ^{58}Ni target was investigated and the coupling to the $^7\text{Be} + p$ ($S_p = 0.138$ MeV) breakup channel has shown to be crucial to describe the data [6–8]. Also, in these works, the halo configuration for ^8B could be established. Elastic scattering of stable and tightly bound ^{10}B and ^{11}B projectiles on ^{58}Ni have been recently investigated [9,10]. In these works, large-scale coupled reaction channel calculations, without any imaginary potential

at the interaction surface, have been used to investigate the relative importance of the different reaction channels on the reaction mechanism. The ^{10}B ($J^\pi = 3^+$) nucleus is bound by $S_\alpha = 4.461$ MeV for the $^6\text{Li} + \alpha$ channel and has a quite large deformation, $Q(^{10}\text{B}) = 8.47$ fm². Reorientation and spin-orbit effects were very important for the description of the elastic scattering of $^{10}\text{B} + ^{58}\text{Ni}$ [9]. The importance of quadrupole deformation and reorientation effects was already observed in the elastic scattering data of ^{10}B and ^{11}B on light ^{27}Al target [11] and also more recently in the $^{10}\text{B} + ^{120}\text{Sn}$ system [12]. These effects were also shown to be important to describe the elastic scattering of ^{11}B projectile on ^{58}Ni at energies close to the Coulomb barrier [10]. Since ^{11}B is a quite tightly bound nucleus with $S_\alpha = 8.664$ MeV, the breakup was not an important channel to be coupled to the elastic and there was almost no contribution from transfer reactions. To complete the systematic study for the elastic scattering of boron isotopes on ^{58}Ni target, we report, for the first time, the measurement and analysis of the elastic scattering angular distribution of the radioactive ^{12}B projectile on ^{58}Ni target, at energies close to the barrier. The ^{12}B ($J^\pi = 1^+$) nucleus is the neutron-rich isotope of the boron chain with binding energy of $S_n = 3.370$ MeV for the $^{11}\text{B} + n$ channel. The newly obtained data are compared to complete coupled channel calculations, where several inelastic channels were included in the coupling matrix, as well as the reorientation, spin-orbit, and transfer channels, the latter through coupled reaction channel (CRC) calculation.

The paper is organized as follows. Section II contains a description of the experiment. Section III presents the data and gives the results of the coupled channel calculations.

Section IV is dedicated to presentation of the coupled reaction channel calculations. Finally, the last section presents a summary of this work.

II. EXPERIMENTAL SETUP AND MEASUREMENTS

Angular distributions of the $^{12}\text{B} + ^{58}\text{Ni}$ elastic scattering were measured at $E_{\text{Lab}} = 30.0$ and 33.0 MeV. The secondary ^{12}B radioactive ion beam was produced by the RIBRAS (Radioactive Ion Beams in Brazil) facility, installed at the 8-UD Pelletron Tandem of the University of São Paulo [13]. The facility consists of two superconducting solenoids with 6.5 T maximum central field and a 30-cm clear warm bore. Although the two solenoids are available, for this measurement only one solenoid was used. The production target was mounted in a chamber before the first solenoid and consisted of a ^9Be foil $14.4 \mu\text{m}$ thick. To produce the secondary ^{12}B beam, we used the $^9\text{Be}(^{11}\text{B}, ^{12}\text{B})^8\text{Be}$ transfer reaction ($Q_{\text{value}} = +1.705$ MeV). The $^{11}\text{B}^{4+}$ primary beam was accelerated by the Pelletron Accelerator at energies of 37.0 and 40.0 MeV, with intensity of typically 300 nAe, producing the secondary ^{12}B beam with an average intensity of 2×10^5 pps. The primary beam (^{11}B) was collected after the production target by a Faraday cup, constituted by an isolated tungsten alloy rod, which stops all particles in the angular range from 0° to 2.7° and integrates the charge. The secondary ^{12}B radioactive beam particles, produced in flight at forward direction, are collected within an angular range of $2.7^\circ \leq \theta_{\text{Lab}} \leq 6.0^\circ$ by the superconducting solenoid and focused into the scattering chamber right after the first solenoid. A system of blocks and collimators, located along the solenoid axes, was used to clean up the beam of interest.

A 2.1 mg/cm^2 thick isotopically enriched ^{58}Ni target was used for the elastic scattering measurements. This target was mounted in a target holder along with a 4.6 mg/cm^2 thick gold target. The gold target was used in separate runs to obtain the overall normalization since elastic scattering at these energies is expected to be Rutherford for the angular range measured.

The detection system consisted of two $\Delta E - E$ telescopes with silicon planar detectors of 25 and $1000 \mu\text{m}$ thicknesses, for the measurements at forward angles, and one $1000\text{-}\mu\text{m}$ -thick E planar silicon detector for measurements at back angles. The telescopes and the E detector had a circular aperture that subtended a solid angle of about 16 msr ($\pm 4.0^\circ$). Since the elastic cross sections in the angular interval covered by these detectors could vary by almost an order of magnitude, the average detection angle was determined by a Monte Carlo simulation, which took into account the detector collimator, the secondary beam-spot dimension on the secondary target (4 mm), the secondary beam divergence (2° to 4°), and the angular distribution in the range of the detector aperture (Rutherford for the gold target and at forward angles for nickel target). This correction is particularly important for the most forward angles.

Although the magnetic field of the solenoid was adjusted to focus the ^{12}B secondary beam and the blocks and collimators were used to prevent particles with different magnetic rigidity from reaching the scattering target, particles with the same magnetic rigidity such as ^9Be , $^{6,7}\text{Li}$, and ^4He were also present

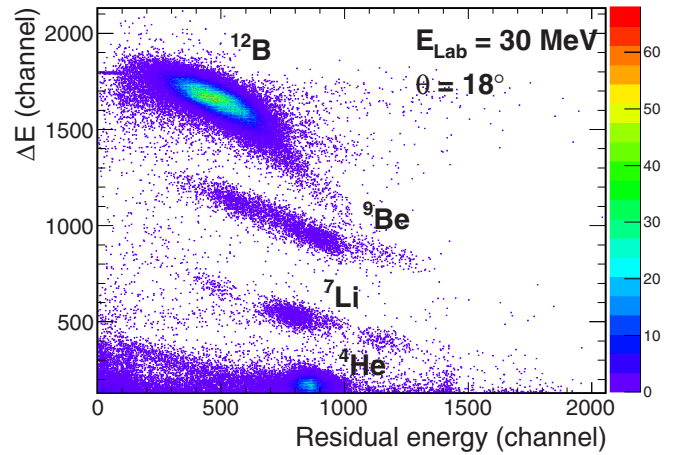


FIG. 1. A typical bidimensional $\Delta E - E$ spectrum for the $^{12}\text{B} + ^{58}\text{Ni}$ measured at $\theta_{\text{Lab}} = 18.0^\circ$ and $E_{\text{Lab}} = 30.0$ MeV. The beam contaminants are indicated.

in the beam cocktail. The different scattering particles were identified using the combination of ΔE and E_{residual} information for the data taken with the telescopes. A selected particle identification in the $\Delta E - E$ spectrum is shown in Fig. 1. In this plot, the scattered ^{12}B and the contaminants ^9Be , $^{6,7}\text{Li}$, and ^4He beams on the nickel target, at 18° , are displayed, clearly separated, and identified. The inelastic scattering ^{11}B primary beam was completely blocked by the system of blocks and collimators and does not appear in the plot. A typical energy spectrum for the single E detector, used for the backward angle measurements, is shown in Fig. 2. The peak corresponding to ^{12}B is the one with highest energy and it could be easily identified. A small background present below the ^{12}B peak could be estimated and considered to obtain the correct yields. The experimental resolution for the ^{12}B beam was about 1.0 to 1.5 MeV, obtained from the FWHM (full width of half maximum) of the peak corresponding to ^{12}B scattered in the gold target.

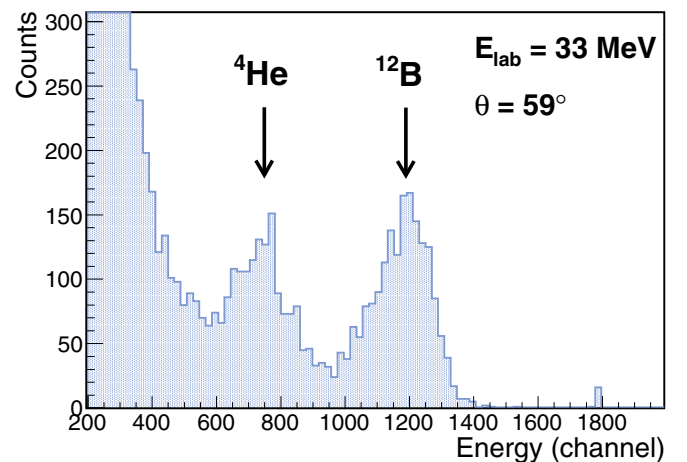


FIG. 2. A typical energy spectra for the $^{12}\text{B} + ^{58}\text{Ni}$ measured at $\theta_{\text{Lab}} = 59.0^\circ$ and $E_{\text{Lab}} = 33.0$ MeV. The peak for the ^{12}B scattering particles is indicated.

TABLE I. Spin parity and energy of the states in ^{58}Ni and ^{12}B , from the NNDC database [17], considered in the coupled channel calculations.

^{58}Ni		^{12}B	
J^π	E (MeV)	J^π	E (MeV)
0^+	g.s.	1^+	g.s.
2^+	1.454		
4^+	2.459		
2^+	2.775		
0^+	2.942		
3^-	4.475		

The angular distributions were measured from $\theta_{\text{Lab}} = 18.0^\circ$ to 65.0° , at 30.0 MeV, and from $\theta_{\text{Lab}} = 26.0^\circ$ to 68.0° , at 33.0 MeV. The uncertainties in the cross sections ranged from 1.5% to 17% starting from most forward to most backward angles, for the $E_{\text{Lab}} = 30.0$ MeV measurement, and 2% to 10% for the $E_{\text{Lab}} = 33.0$ MeV measurement.

III. COUPLED CHANNEL CALCULATIONS

The angular distributions were analyzed in terms of coupled channel (CC) calculations. In this approach, the absorption from the elastic channel is produced by the real process of opening inelastic channels. Here we adopted the parameter-free double-folding São Paulo potential (SPP) [14] as the real bare potential to simulate the nuclear interaction between the projectile and target nuclei. For the energies considered in the present work (close to the barrier), the SPP can be regarded as energy independent, and the relevant feature for the calculations is its double-folding characteristic. Since the interest is to investigate the important channels that affect the elastic scattering angular distributions, no imaginary surface potential was employed in our coupled channel calculation. The relevant reaction channels or effect should then be explicitly taken into account. However, a short-range imaginary potential was considered to simulate the absorption of flux due to fusion, since the fusion channel is not explicitly included in the calculations. This short-range potential had Woods-Saxon shape with the parameters $V_i = 50$ MeV, $r_i = 1.06$ fm, and $a_i = 0.2$ fm. Here, r_i is the reduced radius which should be multiplied by the mass terms ($A_p^{1/3} + A_t^{1/3}$) to give the actual radius of the potential. This set of parameters was obtained from Ref. [15]. Actually, the final results are not very sensitive to this particular choice of parameters. All the calculations were performed using the code FRESKO [16].

TABLE II. All $E2$ inelastic transitions for ^{58}Ni used in the coupled-channel calculations.

E (keV)	E_γ (keV)	$J_F \rightleftharpoons J_i$	$B(E2)$ (W.u.)	$\langle J_f E2 J_i \rangle$ ($e^2 \text{fm}^4$)	δ_2 (fm)
1454.28	1454.28	$0^+ \rightleftharpoons 2^+$	10 (4)	26.365	0.941
2459.21	1004.8	$2^+ \rightleftharpoons 4^+$	11.2 (12)	80.189	2.923
2775.42	2775.42	$2^+ \rightleftharpoons 2^+$	15 (4)	-44.523	-1.623
2942.56	167.2	$2^+ \rightleftharpoons 0^+$	21 (3)	16.667	0.608

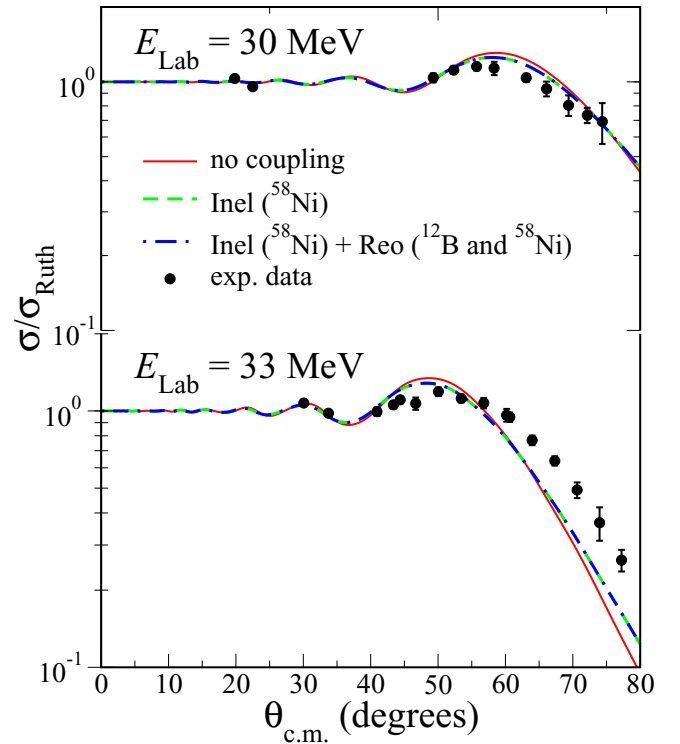


FIG. 3. Elastic scattering angular distributions for the $^{12}\text{B} + ^{58}\text{Ni}$ system at $E_{\text{Lab}} = 30.0$ and 33.0 MeV. The lines are results of coupled channel calculations as indicated.

The angular distributions at 30.0 and 33.0 MeV for the $^{12}\text{B} + ^{58}\text{Ni}$ system have been analyzed with coupled channel calculations. Only the influence of the ^{58}Ni excited states in the elastic scattering was considered in the calculations. The ground state of ^{12}B has $J^\pi = 1^+$ and the two first excited states are the 0.953 MeV ($J^\pi = 2^+$) and 1.674 MeV ($J^\pi = 2^-$) states. The transition between the first excited state to ground state, $2^+ \rightarrow 1^+$, is an $M1$ transition in nature and thus very weak. The transition of second excited state and ground state, $2^- \rightarrow 1^+$, is an $E1$ transition but also very weak according to the NNDC database [17]. The spin, parity, and energy of the excited states of the ^{58}Ni target used in the calculations were obtained from NNDC database [17] and are listed in Table I.

In the present CC calculation, the excited states in ^{58}Ni were considered to be collective in nature, and the $E2$ transitions with no change in parity, as given by the 1.454 MeV (2^+) one-phonon singlet and by the 2.459 (4^+), 2.775 (2^+), and 2.943 (0^+) two-phonon triplet, were calculated within the vibrational model. The $B(E2)$ experimental

TABLE III. The $E3$ inelastic transition for ^{58}Ni used in the coupled-channel calculations.

E (keV)	E_γ (keV)	$J_f \rightleftharpoons J_i$	$B(E3)$ ($\text{e}^2 \text{b}^3$)	$\langle J_f E3 J_i \rangle$ ($\text{e}^2 \text{fm}^4$)	δ_3 (fm)
4474.6	4474.6	$0^+ \rightleftharpoons 3^-$	0.0195 (27)	112.443	0.9991

values available in NNDC for these states in ^{58}Ni are listed in Table II. The state at 4.475 (3^-), which could be of some importance in the coupled channel scheme since it is a one-phonon $E3$ transition to the ground state, was also included. The $B(E3)$ experimental value from NNDC for this state in ^{58}Ni is listed in Table III. The states between 2.943 and 4.475 MeV in ^{58}Ni are expected to give weak couplings and were not considered in our calculations.

The comparison of results of the CC calculation with the data taken at 30.0 and 33.0 MeV is shown in Fig. 3. In this figure, the red solid line corresponds to the cross sections from the CC calculation when all the inelastic channels are left out in CC calculations (no coupling) and the green dashed line represents the results when all states of the target are included in the coupling matrix. As can be observed in the figure, the effect of the couplings is small but it is in the direction of reducing the cross sections at the Fresnel peak and increasing the elastic cross sections at backward angles.

Despite the inclusion of almost all excited states of the target in the calculation, our coupled channel calculations did not agree with the measured elastic cross sections at 33.0 MeV. To improve the agreement, the reorientation channels for the ground state of ^{12}B and the first excited state of ^{58}Ni were

also included in the coupling matrix. These effects have been shown to be quite important to describe the elastic scattering of $^{10,11}\text{B} + ^{58}\text{Ni}$ data [9,10] and $^{10}\text{B} + ^{120}\text{Sn}$ [12]. The spin reorientation of the ground state of ^{12}B and first excited state of ^{58}Ni , as indicated in Table IV, were considered. The results of the CC calculations with these effects are also shown in Fig. 3. As observed in the figure, the effect of the spin reorientation of both projectile and target has minor or almost no influence in cross sections. This might be mainly due to the small deformation of ^{12}B , $Q_2 = 1.32(2) \text{ fm}^2$ [18]. We would like to emphasize once more that these calculations are parameter-free and no artificial superficial imaginary potential has been used.

IV. COUPLED REACTION CHANNEL (CRC) CALCULATIONS

From the analysis presented in the previous section, it is clear that the inelastic couplings and spin reorientation were not sufficient to reproduce the experimental elastic data at 33.0 MeV. This is an indication that other channels

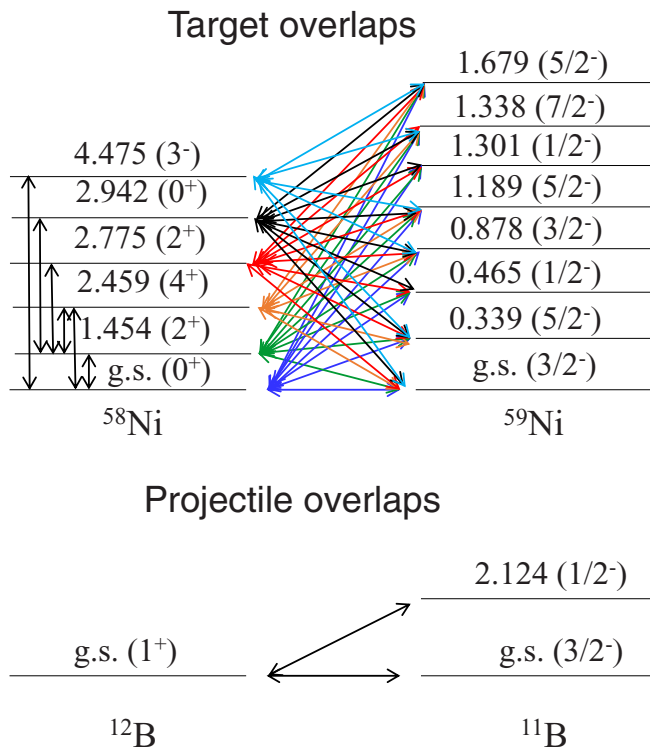


FIG. 4. Coupling scheme of the projectile and target overlaps used in the one-neutron stripping transfer reaction.

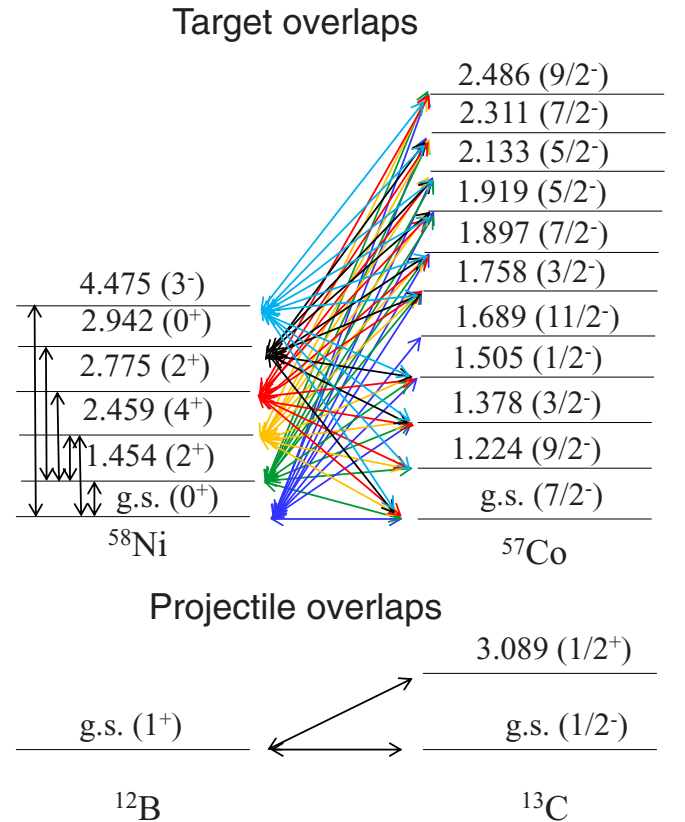


FIG. 5. Coupling scheme of the projectile and target overlaps used in the one-proton pickup transfer reaction.

TABLE IV. Reorientation parameters used in the coupled channel calculations.

Nucleus	E_{level} (MeV)	J^π	Q_2 (fm ²)	$\langle J_f E2 J_i \rangle$ (e ² fm ⁴)	δ_2 (fm)	β_2
^{12}B	g.s.	1^+	+1.32 (6)	0.228	0.040	0.03
^{58}Ni	1.4542	2^+	-10 (6)	-31.481	-1.477	0.234

such as transfer and/or breakup reactions have been open at this energy. In this section, we investigated the effect of two transfer channels: one-neutron stripping (^{12}B , ^{11}B) and one-proton pickup (^{12}B , ^{13}C) reactions. These are transfer channels with low-mass transfer particles and with positive $Q_{\text{value}} = +5.629$ MeV and $+9.360$ MeV, respectively. To take into account these transfer reactions, we have to consider exact finite-range coupled reaction channel (CRC) calculations. For this purpose, double-folding São Paulo Potential (SPP) [14] was used for the real part optical potential of the entrance partition and a Woods-Saxon for the imaginary part, with depth, radius, and diffuseness given by $V = 50$ MeV, $r_i = 1.06$ fm, and $a_i = 0.2$ fm, respectively. This was exactly the same optical potential used in the previous section for

the coupled channel calculations, including only the inelastic excitation of the target. In the outgoing partition, the imaginary part was assumed to have the same radial dependence of the real part, but multiplied by strength coefficient $N_I = 0.78$, because no couplings were explicitly considered. These parameters have already shown to be suitable for describing elastic scattering cross sections for many systems [19] at energies above the Coulomb barrier, where no relevant couplings to the elastic channel are expected. Another important ingredient in these one-neutron and one-proton transfer reactions calculations is the potentials which bind the transferred particles in the projectile and target cores, used to calculate the internal single-particle wave functions. Here, these wave functions were generated by considering Woods-Saxon form

TABLE V. Spectroscopic amplitudes used in the CRC calculations for one neutron transfer using the model space p with the effective phenomenological $pmom$ [21] interaction for projectile overlap and model space $bjuff$ with the effective phenomenological $48Cauff$ [22] interaction for target overlap.

Initial state	Final state	nlj	Spect. ampl.
$^{12}\text{B}_{g.s.}(1^+)$	$^{11}\text{B}_{g.s.}(3/2^-)$	$1p_{1/2}$	-0.868
		$1p_{3/2}$	0.326
$^{12}\text{B}_{g.s.}(1^+)$	$^{11}\text{B}_{2.124}(1/2^-)$	$1p_{1/2}$	-0.099
		$1p_{3/2}$	0.514
$^{58}\text{Ni}_{g.s.}(0^+)$	$^{59}\text{Ni}_{g.s.}(3/2^-)$	$2p_{3/2}$	0.709
$^{58}\text{Ni}_{g.s.}(0^+)$	$^{59}\text{Ni}_{0.339}(5/2^-)$	$1f_{5/2}$	-0.785
$^{58}\text{Ni}_{g.s.}(0^+)$	$^{59}\text{Ni}_{0.465}(1/2^-)$	$2p_{1/2}$	0.491
$^{58}\text{Ni}_{g.s.}(0^+)$	$^{59}\text{Ni}_{0.877}(3/2^-)$	$2p_{3/2}$	-0.310
$^{58}\text{Ni}_{g.s.}(0^+)$	$^{59}\text{Ni}_{1.189}(5/2^-)$	$1f_{5/2}$	-0.089
$^{58}\text{Ni}_{g.s.}(0^+)$	$^{59}\text{Ni}_{1.301}(1/2^-)$	$2p_{1/2}$	-0.567
$^{58}\text{Ni}_{g.s.}(0^+)$	$^{59}\text{Ni}_{1.679}(5/2^-)$	$1f_{5/2}$	0.242
$^{58}\text{Ni}_{1.454}(2^+)$	$^{59}\text{Ni}_{g.s.}(3/2^-)$	$2p_{1/2}$	0.021
		$2p_{3/2}$	-0.810
		$1f_{5/2}$	-0.211
$^{58}\text{Ni}_{1.454}(2^+)$	$^{59}\text{Ni}_{0.339}(5/2^-)$	$2p_{1/2}$	0.044
		$2p_{3/2}$	0.219
		$1f_{5/2}$	-0.229
$^{58}\text{Ni}_{1.454}(2^+)$	$^{59}\text{Ni}_{0.465}(1/2^-)$	$2p_{3/2}$	-0.764
		$1f_{5/2}$	0.576
		$2p_{1/2}$	-0.386
$^{58}\text{Ni}_{1.454}(2^+)$	$^{59}\text{Ni}_{0.877}(3/2^-)$	$2p_{3/2}$	-0.545
		$1f_{5/2}$	-0.626
		$2p_{1/2}$	0.425
$^{58}\text{Ni}_{1.454}(2^+)$	$^{59}\text{Ni}_{1.189}(5/2^-)$	$2p_{3/2}$	-0.753
		$1f_{5/2}$	0.002
		$2p_{1/2}$	-0.156
$^{58}\text{Ni}_{1.454}(2^+)$	$^{59}\text{Ni}_{1.301}(1/2^-)$	$2p_{3/2}$	-0.156
		$1f_{5/2}$	0.613

TABLE V. (Continued.)

Initial state	Final state	nlj	Spect. ampl.
$^{58}\text{Ni}_{1.454}(2^+)$	$^{59}\text{Ni}_{1.338}(7/2^-)$	$2p_{3/2}$	0.006
		$1f_{5/2}$	-0.798
$^{58}\text{Ni}_{1.454}(2^+)$	$^{59}\text{Ni}_{1.679}(5/2^-)$	$2p_{1/2}$	0.229
		$2p_{3/2}$	0.031
		$1f_{5/2}$	-0.755
$^{58}\text{Ni}_{2.459}(4^+)$	$^{59}\text{Ni}_{g.s.}(3/2^-)$	$1f_{5/2}$	-0.389
$^{58}\text{Ni}_{2.459}(4^+)$	$^{59}\text{Ni}_{0.339}(5/2^-)$	$2p_{3/2}$	-0.807
		$1f_{5/2}$	-0.155
$^{58}\text{Ni}_{2.459}(4^+)$	$^{59}\text{Ni}_{0.877}(3/2^-)$	$1f_{5/2}$	0.542
$^{58}\text{Ni}_{2.459}(4^+)$	$^{59}\text{Ni}_{1.189}(5/2^-)$	$2p_{3/2}$	0.002
		$1f_{5/2}$	-0.494
$^{58}\text{Ni}_{2.459}(4^+)$	$^{59}\text{Ni}_{1.338}(7/2^-)$	$2p_{1/2}$	0.039
		$2p_{3/2}$	0.671
		$1f_{5/2}$	0.475
$^{58}\text{Ni}_{2.459}(4^+)$	$^{59}\text{Ni}_{1.679}(5/2^-)$	$2p_{3/2}$	-0.265
		$1f_{5/2}$	0.142
$^{58}\text{Ni}_{2.775}(2^+)$	$^{59}\text{Ni}_{g.s.}(3/2^-)$	$2p_{1/2}$	-0.385
		$2p_{3/2}$	-0.608
		$1f_{5/2}$	0.011
$^{58}\text{Ni}_{2.775}(2^+)$	$^{59}\text{Ni}_{0.339}(5/2^-)$	$2p_{1/2}$	-0.194
		$2p_{3/2}$	-0.064
		$1f_{5/2}$	-0.304
$^{58}\text{Ni}_{2.775}(2^+)$	$^{59}\text{Ni}_{0.465}(1/2^-)$	$2p_{3/2}$	0.668
		$1f_{5/2}$	0.095
		$2p_{1/2}$	-0.121
$^{58}\text{Ni}_{2.775}(2^+)$	$^{59}\text{Ni}_{0.877}(3/2^-)$	$2p_{3/2}$	0.157
		$1f_{5/2}$	0.195
		$2p_{1/2}$	0.448
$^{58}\text{Ni}_{2.775}(2^+)$	$^{59}\text{Ni}_{1.189}(5/2^-)$	$2p_{3/2}$	0.602
		$1f_{5/2}$	-0.229
		$2p_{1/2}$	0.448

TABLE V. (*Continued.*)

Initial state	Final state	nlj	Spect. ampl.
$^{58}\text{Ni}_{2.775}(2^+)$	$^{59}\text{Ni}_{1.301}(1/2^-)$	$2p_{3/2}$	-0.211
		$1f_{5/2}$	-0.187
$^{58}\text{Ni}_{2.775}(2^+)$	$^{59}\text{Ni}_{1.338}(7/2^-)$	$2p_{3/2}$	0.184
		$1f_{5/2}$	-0.299
$^{58}\text{Ni}_{2.775}(2^+)$	$^{59}\text{Ni}_{1.679}(5/2^-)$	$2p_{1/2}$	0.113
		$2p_{3/2}$	-0.012
		$1f_{5/2}$	-0.044
$^{58}\text{Ni}_{2.942}(0^+)$	$^{59}\text{Ni}_{g.s.}(3/2^-)$	$2p_{3/2}$	0.089
$^{58}\text{Ni}_{2.942}(0^+)$	$^{59}\text{Ni}_{0.339}(5/2^-)$	$1f_{5/2}$	0.242
$^{58}\text{Ni}_{2.942}(0^+)$	$^{59}\text{Ni}_{0.465}(1/2^-)$	$2p_{1/2}$	-0.358
$^{58}\text{Ni}_{2.942}(0^+)$	$^{59}\text{Ni}_{0.877}(3/2^-)$	$2p_{3/2}$	-0.491
$^{58}\text{Ni}_{2.942}(0^+)$	$^{59}\text{Ni}_{1.189}(5/2^-)$	$1f_{5/2}$	-0.153
$^{58}\text{Ni}_{2.942}(0^+)$	$^{59}\text{Ni}_{1.301}(1/2^-)$	$2p_{1/2}$	-0.147
$^{58}\text{Ni}_{2.942}(0^+)$	$^{59}\text{Ni}_{1.679}(5/2^-)$	$1f_{5/2}$	0.222
$^{58}\text{Ni}_{4.475}(3^-)$	$^{59}\text{Ni}_{g.s.}(3/2^-)$	$1g_{9/2}$	0.026
$^{58}\text{Ni}_{4.475}(3^-)$	$^{59}\text{Ni}_{0.339}(5/2^-)$	$1g_{9/2}$	0.011
$^{58}\text{Ni}_{4.475}(3^-)$	$^{59}\text{Ni}_{0.877}(3/2^-)$	$1g_{9/2}$	-0.064
$^{58}\text{Ni}_{4.475}(3^-)$	$^{59}\text{Ni}_{1.189}(5/2^-)$	$1g_{9/2}$	-0.046
$^{58}\text{Ni}_{4.475}(3^-)$	$^{59}\text{Ni}_{1.338}(7/2^-)$	$1g_{9/2}$	-0.036
$^{58}\text{Ni}_{4.475}(3^-)$	$^{59}\text{Ni}_{1.679}(5/2^-)$	$1g_{9/2}$	0.015

factors with reduced radii and diffuseness as $r_0 = 1.25$ fm and $a = 0.65$ fm, respectively, for the ^{12}B , ^{11}B , ^{58}Ni , ^{13}C , ^{57}Co , and ^{57}Ni nuclei. The depths of the Woods-Saxon potentials were varied to reproduce the experimental binding energies for one neutron and one proton in the respective core.

The full complex remnant in coupling matrix elements, prior representation, and nonorthogonality corrections were adopted in the full CRC calculations. The influence of the one-neutron striping (^{12}B , ^{11}B) and one-proton pickup (^{12}B , ^{13}C) reactions on the elastic scattering was separately studied. The transfer schemes considered for both one neutron and one proton in the present CRC calculations are shown in Figs. 4 and 5, respectively. The amplitudes for the projectile and target overlaps used in the microscopic CRC calculations were obtained by shell model calculations. These spectroscopic amplitudes were derived using the NUSHELLX code [20]. To obtain the one-neutron spectroscopic information of the projectile overlaps, the p model space and effective interaction $pmom$ [21] were used. In this model space, the ^4He nucleus is considered as a closed core and the $1p_{1/2}$ and $1p_{3/2}$ orbitals are taken as valence subspace for both neutrons and protons. For the target overlaps, the $bjuff$ model space and effective interaction $48Cauff$ [22] were used for one-neutron transfer. In this model space, the ^{48}Ca nucleus is considered as a closed core and the $1f_{7/2}$ and $2p_{3/2}$ orbital valences for protons and the $2p_{3/2}$, $1f_{5/2}$, $2p_{1/2}$, and $1g_{9/2}$ orbital valences for neutrons were used. In Table V, the spectroscopic amplitudes used in the one-neutron pickup transfer reactions, concerning the projectile and target overlaps, are shown.

For one-proton transfer, the fp model space and effective interaction $fpd6cdpn$ [23] were used. In this model subspace, the ^{40}Ca nucleus is considered as a closed core and the $1f_{7/2}$,

TABLE VI. Spectroscopic amplitudes used in the CRC calculations for one proton transfer using the model space p with the effective phenomenological $pmom$ [21] interaction for projectile overlap and model space fp with the effective phenomenological $fpd6cdpn$ [23] interaction for target overlap.

Initial state	Final state	nlj	Spect. ampl.
$^{12}\text{B}_{g.s.}(1^+)$	$^{13}\text{C}_{g.s.}(1/2^-)$	$1p_{1/2}$	0.077
		$1p_{3/2}$	-1.105
$^{58}\text{Ni}_{g.s.}(0^+)$	$^{57}\text{Co}_{g.s.}(7/2^-)$	$1f_{7/2}$	-2.252
$^{58}\text{Ni}_{g.s.}(0^+)$	$^{57}\text{Co}_{1.378}(3/2^-)$	$2p_{3/2}$	0.232
$^{58}\text{Ni}_{g.s.}(0^+)$	$^{57}\text{Co}_{1.505}(1/2^-)$	$2p_{1/2}$	0.033
$^{58}\text{Ni}_{g.s.}(0^+)$	$^{57}\text{Co}_{1.758}(3/2^-)$	$2p_{3/2}$	0.341
$^{58}\text{Ni}_{g.s.}(0^+)$	$^{57}\text{Co}_{1.897}(7/2^-)$	$1f_{7/2}$	-0.804
$^{58}\text{Ni}_{g.s.}(0^+)$	$^{57}\text{Co}_{1.919}(5/2^-)$	$1f_{5/2}$	-0.090
$^{58}\text{Ni}_{g.s.}(0^+)$	$^{57}\text{Co}_{2.133}(5/2^-)$	$1f_{5/2}$	-0.252
$^{58}\text{Ni}_{g.s.}(0^+)$	$^{57}\text{Co}_{2.311}(7/2^-)$	$1f_{7/2}$	-0.172
$^{58}\text{Ni}_{1.454}(2^+)$	$^{57}\text{Co}_{g.s.}(7/2^-)$	$2p_{3/2}$	-0.232
		$1f_{5/2}$	-0.085
		$1f_{7/2}$	0.569
$^{58}\text{Ni}_{1.454}(2^+)$	$^{57}\text{Co}_{1.224}(9/2^-)$	$1f_{5/2}$	-0.013
		$1f_{7/2}$	-0.992
$^{58}\text{Ni}_{1.454}(2^+)$	$^{57}\text{Co}_{1.378}(3/2^-)$	$2p_{1/2}$	0.047
		$2p_{3/2}$	0.083
		$1f_{5/2}$	0.058
		$1f_{7/2}$	0.090
$^{58}\text{Ni}_{1.454}(2^+)$	$^{57}\text{Co}_{1.505}(1/2^-)$	$2p_{3/2}$	-0.050
		$1f_{5/2}$	0.075
$^{58}\text{Ni}_{1.454}(2^+)$	$^{57}\text{Co}_{1.758}(3/2^-)$	$2p_{1/2}$	0.033
		$2p_{3/2}$	-0.041
		$1f_{5/2}$	0.014
		$1f_{7/2}$	0.660
$^{58}\text{Ni}_{1.454}(2^+)$	$^{57}\text{Co}_{1.897}(7/2^-)$	$2p_{3/2}$	-0.078
		$1f_{5/2}$	-0.038
		$1f_{7/2}$	-0.586
$^{58}\text{Ni}_{1.454}(2^+)$	$^{57}\text{Co}_{1.919}(5/2^-)$	$2p_{1/2}$	-0.029
		$2p_{3/2}$	0.069
		$1f_{5/2}$	-0.077
		$1f_{7/2}$	-0.699
$^{58}\text{Ni}_{1.454}(2^+)$	$^{57}\text{Co}_{2.133}(5/2^-)$	$2p_{1/2}$	-0.026
		$2p_{3/2}$	0.115
		$1f_{5/2}$	-0.089
$^{58}\text{Ni}_{1.454}(2^+)$	$^{57}\text{Co}_{2.311}(7/2^-)$	$1f_{7/2}$	0.530
		$2p_{3/2}$	-0.018
$^{58}\text{Ni}_{1.454}(2^+)$	$^{57}\text{Co}_{2.311}(7/2^-)$	$1f_{5/2}$	-0.001
		$1f_{7/2}$	0.569
		$1f_{5/2}$	-0.053
$^{58}\text{Ni}_{1.454}(2^+)$	$^{57}\text{Co}_{2.486}(9/2^-)$	$1f_{5/2}$	-0.053
		$1f_{7/2}$	0.694
$^{58}\text{Ni}_{1.454}(2^+)$	$^{57}\text{Co}_{g.s.}(7/2^-)$	$2p_{1/2}$	0.029
		$2p_{3/2}$	0.034
		$1f_{5/2}$	0.049
		$1f_{7/2}$	-0.026
$^{58}\text{Ni}_{1.454}(2^+)$	$^{57}\text{Co}_{1.224}(9/2^-)$	$2p_{1/2}$	-0.004
		$2p_{3/2}$	-0.063
		$1f_{5/2}$	-0.324
		$1f_{7/2}$	-0.537

TABLE VI. (Continued.)

Initial state	Final state	nlj	Spect. ampl.
$^{58}\text{Ni}_{2,459}(4^+)$	$^{57}\text{Co}_{1,378}(3/2^-)$	$1f_{5/2}$	-0.079
		$1f_{7/2}$	-0.004
$^{58}\text{Ni}_{2,459}(4^+)$	$^{57}\text{Co}_{1,505}(1/2^-)$	$1f_{7/2}$	-0.022
$^{58}\text{Ni}_{2,459}(4^+)$	$^{57}\text{Co}_{1,758}(3/2^-)$	$1f_{5/2}$	0.003
		$1f_{7/2}$	0.164
$^{58}\text{Ni}_{2,459}(4^+)$	$^{57}\text{Co}_{1,897}(7/2^-)$	$2p_{1/2}$	0.025
		$2p_{3/2}$	-0.055
		$1f_{5/2}$	0.014
		$1f_{7/2}$	-0.647
$^{58}\text{Ni}_{2,459}(4^+)$	$^{57}\text{Co}_{1,919}(5/2^-)$	$2p_{3/2}$	-0.053
		$1f_{5/2}$	0.045
		$1f_{7/2}$	0.311
$^{58}\text{Ni}_{2,459}(4^+)$	$^{57}\text{Co}_{2,133}(5/2^-)$	$2p_{3/2}$	-0.044
		$1f_{5/2}$	0.034
		$1f_{7/2}$	0.206
$^{58}\text{Ni}_{2,459}(4^+)$	$^{57}\text{Co}_{2,311}(7/2^-)$	$2p_{1/2}$	0.006
		$2p_{3/2}$	0.005
		$1f_{5/2}$	0.014
		$1f_{7/2}$	-0.647
$^{58}\text{Ni}_{2,775}(2^+)$	$^{57}\text{Co}_{g,s}(7/2^-)$	$2p_{3/2}$	0.024
		$1f_{5/2}$	-0.007
		$1f_{7/2}$	-0.006
$^{58}\text{Ni}_{2,775}(2^+)$	$^{57}\text{Co}_{1,224}(9/2^-)$	$1f_{5/2}$	0.020
		$1f_{7/2}$	0.111
$^{58}\text{Ni}_{2,775}(2^+)$	$^{57}\text{Co}_{1,378}(3/2^-)$	$2p_{1/2}$	-0.002
		$2p_{3/2}$	0.002
		$1f_{5/2}$	-0.017
		$1f_{7/2}$	-0.003
$^{58}\text{Ni}_{2,775}(2^+)$	$^{57}\text{Co}_{1,505}(1/2^-)$	$2p_{3/2}$	0.007
		$1f_{5/2}$	-0.020
$^{58}\text{Ni}_{2,775}(2^+)$	$^{57}\text{Co}_{1,758}(3/2^-)$	$2p_{1/2}$	0.012
		$2p_{3/2}$	0.016
		$1f_{5/2}$	0.003
		$1f_{7/2}$	-0.111
$^{58}\text{Ni}_{2,775}(2^+)$	$^{57}\text{Co}_{1,897}(7/2^-)$	$2p_{3/2}$	0.007
		$1f_{5/2}$	0.018
		$1f_{7/2}$	0.057
$^{58}\text{Ni}_{2,775}(2^+)$	$^{57}\text{Co}_{1,919}(5/2^-)$	$2p_{1/2}$	0.007
		$2p_{3/2}$	-0.025
		$1f_{5/2}$	0.025
		$1f_{7/2}$	0.078
$^{58}\text{Ni}_{2,775}(2^+)$	$^{57}\text{Co}_{2,133}(5/2^-)$	$2p_{1/2}$	0.011
		$2p_{3/2}$	0.006
		$1f_{5/2}$	0.003
		$1f_{7/2}$	-0.058
$^{58}\text{Ni}_{2,775}(2^+)$	$^{57}\text{Co}_{2,311}(7/2^-)$	$2p_{3/2}$	0.069
		$1f_{5/2}$	0.062
		$1f_{7/2}$	-0.561
$^{58}\text{Ni}_{2,775}(2^+)$	$^{57}\text{Co}_{2,486}(9/2^-)$	$1f_{5/2}$	0.020
		$1f_{7/2}$	0.688
$^{58}\text{Ni}_{2,942}(0^+)$	$^{57}\text{Co}_{g,s}(7/2^-)$	$1f_{7/2}$	0.047
$^{58}\text{Ni}_{2,942}(0^+)$	$^{57}\text{Co}_{1,378}(3/2^-)$	$2p_{3/2}$	-0.024

TABLE VI. (Continued.)

Initial state	Final state	nlj	Spect. ampl.
$^{58}\text{Ni}_{2,942}(0^+)$	$^{57}\text{Co}_{1,505}(1/2^-)$	$2p_{1/2}$	0.009
$^{58}\text{Ni}_{2,942}(0^+)$	$^{57}\text{Co}_{1,758}(3/2^-)$	$2p_{3/2}$	-0.076
$^{58}\text{Ni}_{2,942}(0^+)$	$^{57}\text{Co}_{1,897}(7/2^-)$	$1f_{7/2}$	0.278
$^{58}\text{Ni}_{2,942}(0^+)$	$^{57}\text{Co}_{1,919}(5/2^-)$	$1f_{5/2}$	-0.020
$^{58}\text{Ni}_{2,942}(0^+)$	$^{57}\text{Co}_{2,133}(5/2^-)$	$1f_{5/2}$	-0.038
$^{58}\text{Ni}_{2,942}(0^+)$	$^{57}\text{Co}_{2,311}(7/2^-)$	$1f_{7/2}$	-1.581

$1f_{5/2}$, $2p_{3/2}$, and $2p_{1/2}$ orbitals are taken as valence subspace for both neutrons and protons. As the $1g_{9/2}$ orbital was not considered in valence subspace for protons, the overlaps of the $^{58}\text{Ni}_{4,475}(3^-)$ state with all states considered in ^{57}Co were missing. However, in order to verify the relevance of these missing couplings, we considered spectroscopic amplitudes for these overlaps equal to 1.0. For the overlap between $^{58}\text{Ni}_{g,s}(0^+)$ with $^{57}\text{Co}_{1,689}(11/2^-)$ state, the spectroscopic amplitudes could be obtained if the $1h_{11/2}$ orbital is considered. So, in order to examine the effect of this overlap in the elastic scattering cross sections of ^{12}B , we have included it in CRC calculations considering spectroscopic amplitudes equal to 1.0. Nevertheless, the addition of these overlaps did not produce any considerable effect on the elastic scattering cross sections of ^{12}B . In Table VI, the spectroscopic amplitudes used in the one-proton transfer reaction, concerning the projectile and target overlaps are shown. For the one-proton transfer, the optimal Q_{value} and energy (E_{opt}) populated were determined using the prescription proposed by Brink [24]. The E_{opt} found for the proton transfer were -4.17 MeV.

The results of CRC calculations including the one-neutron stripping and one-proton pickup reactions are shown in Fig. 6. The red solid lines corresponds to the results of no coupling, while the blue dashed line corresponds to the calculations present in the previous section, with the inclusion of the inelastic and spin reorientation. The inclusion of the one-proton transfer channel to the previous CC calculation is represented by the dash-dotted green line, while the inclusion of the one-neutron channel in the previous CC calculation is given by the thick black line. From Fig. 6, one observes that the effect of one-proton transfer channel on the elastic cross section is negligible. However, the one-neutron transfer channel has been shown to be of some relevance to describe the elastic scattering. It should be emphasized that proton pickup is one of the most favorable transfer channel from the energetic point of view. In addition, all other charged particles will be more massive than the proton and, as usual, the transfers of these charged particles will be even less probable than the proton pickup. In the case of α particles, this is due not only to its higher mass but also due to its greater electrical repulsion. To verify the influence of other transfer channels such as $2n$ stripping, $2p$, deuteron, and α pickup transfer reactions, CRC calculations for these channels were performed considering the cluster model with spectroscopic amplitudes set to 1.0 and, in fact, these channels have very little influence on the elastic scattering of the system investigated. The agreement of the full coupling calculation with the data at 30.0 MeV is

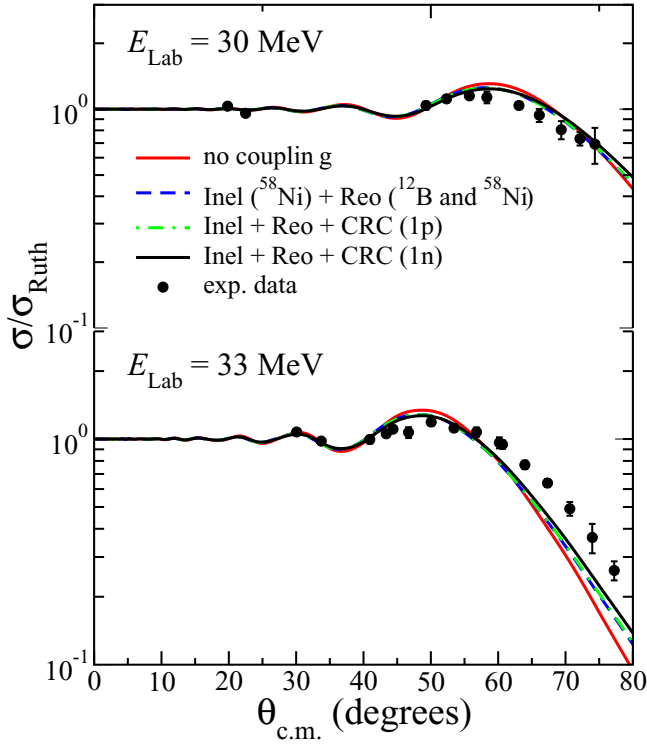


FIG. 6. Elastic scattering angular distributions for the $^{12}\text{B} + ^{58}\text{Ni}$ system at $E_{\text{Lab}} = 30.0$ and 33.0 MeV. The lines are results of coupled reaction channel calculations as indicated.

good. However, the agreement for the angular distribution at 33.0 MeV can be considered only reasonable, indicating that some other channel might be missing in the coupling scheme for the higher energy measurement. We actually checked for the possible influence of the breakup channel in the elastic scattering by performing the continuum discretization coupled channel (CDCC) calculations. The results with and without the coupling to continuum were exactly the same, indicating a negligible influence of this channel.

Since our calculations presented so far have not provided good agreement with the angular distribution at 33.0 MeV, another phenomenon that could be investigated was the spin-orbit coupling. For a long time, this phenomenon has been invoked to explain the elastic scattering of systems involving light nonzero spin projectiles, such as $^{6,7}\text{Li}$, $^{10,11}\text{B}$, and ^{13}C [5,25–30]. In particular, the elastic scattering measurement of polarized ^6Li beams provided strong evidence that spin-orbit coupling is indeed very important for light targets such as ^{12}C and ^{16}O [26]. On the other hand, the intensity of this coupling decreases as the mass of the target increases [26]. However, Weiss *et al.* showed that even in the $^6\text{Li} + ^{58}\text{Ni}$ system there are still indications of spin-orbit coupling [26]. Therefore, although our experiment is not ideal for a detailed study of this important phenomenon, we have done an investigation of what would be its possible influence in our system.

The parameters for the spin-orbit potential are not well known and can be only well defined with analyzing power data. Here, we adopted the radial form factor as the deriva-

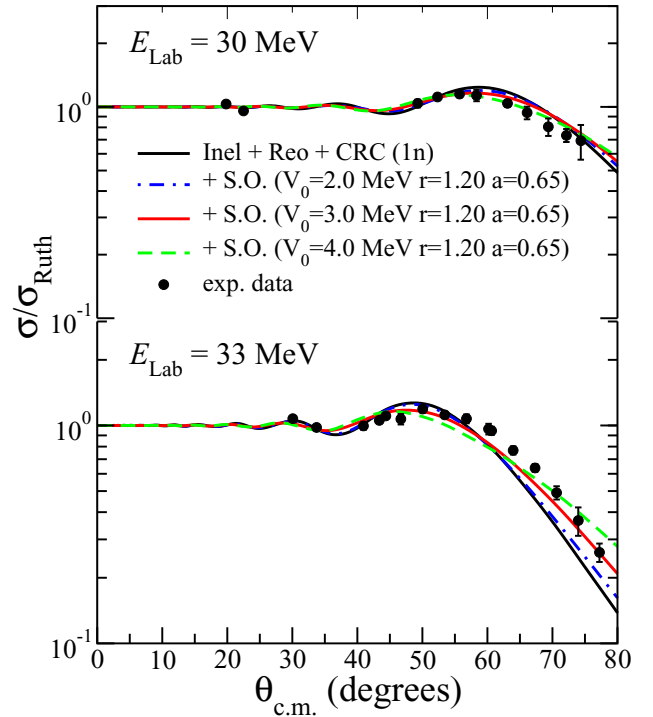


FIG. 7. Elastic scattering angular distribution for the $^{12}\text{B} + ^{58}\text{Ni}$ system at $E_{\text{Lab}} = 30.0$ and 33.0 MeV. The lines corresponds to the inclusion of spin-orbit potential in the calculations.

tive of Woods-Saxon shape with the geometric parameters $r_{SO} = 1.20$ fm and $a_{SO} = 0.65$ fm, where r_{SO} is the reduced radius and a_{SO} is the diffuseness. Since the strength of this potential is not well known, we varied the depth parameter considering the values $V_0 = 2.0, 3.0,$ and 4.0 MeV. The result of inclusion of this term can be seen in Fig. 7. For the angular distribution measured at 30.0 MeV, this term was not strong. However, for the angular distribution at 33.0 MeV, the spin-orbit term improved the agreement of the calculation with the data. Better results were found with the value $V_0 = 3.0$ MeV, which is consistent with the result obtained previously for the $^{10}\text{B} + ^{58}\text{Ni}$ system [9]. Also, there is a possibility that we may be compensating in part for some missing channels or other effects with the inclusion of this spin-orbit potential in the calculation.

V. SUMMARY AND CONCLUSIONS

Angular distributions for elastic scattering of ^{12}B on ^{58}Ni have been measured for the first time at energies close to the barrier, namely 30.0 and 33.0 MeV. The obtained angular distributions have been analyzed in terms of large-scale coupled reaction channel calculations, where several inelastic transitions of the target, as well as one-neutron and one-proton transfer reactions, were included in the coupling matrix. The roles of the spin reorientation of the ^{12}B and ^{58}Ni in the reaction mechanisms were investigated and can be considered negligible. The calculations performed for the coupled channel and reaction channel here can be considered to be parameter free. The real part of the interaction potential

between projectile and target was represented by a parameter-free double-folding potential, and no imaginary potential at the surface was considered. The results of the calculation were compared to the experimental data to investigate the relative importance of the different effects and reaction channels. The inelastic channel, spin reorientation, was found to have negligible influence on the elastic scattering, as expected since ^{12}B has small spin and deformation. Some contribution to the dynamic of the reaction was found for the one-neutron transfer, which have a positive Q_{value} . The agreement of the full coupling calculation with the data at 30.0 MeV is good but there is a clear indication that some other effect or channel might be missing to better describe the angular distribution at 33.0 MeV. With the inclusion of a spin-orbit term, the

agreement of the calculations with the data at 33.0 MeV can be considered good.

ACKNOWLEDGMENTS

The authors would like to thank São Paulo Research Foundation (FAPESP) (Grants No. 2016/02864-4, No. 2016/17612-7, No. 2016/21434-7, and No. 2013/22100-7) and the Conselho Nacional de Desenvolvimento Científico (CNPq) (Grant No. 304961/2017-5) for the financial support. The authors also thank INCT-FNA (Instituto Nacional de Ciência e Tecnologia-Física Nuclear e Aplicações) for support.

-
- [1] J. J. Kolata, V. Guimarães, and E. F. Aguilera, *Eur. Phys. J. A* **52**, 123 (2016).
- [2] L. F. Canto, P. R. S. Gomes, R. Donangelo, J. Lubian, and M. S. Hussein, *Phys. Rep.* **596**, 1 (2015).
- [3] G. R. Satchler, *Nucl. Phys. A* **45**, 197 (1963).
- [4] G. R. Satchler and C. B. Fulmer, *Phys. Lett. B* **50**, 309 (1974).
- [5] K. Rusek, Z. Moroz, R. Caplar, P. Egelhof, K.-H. Möbius, E. Steffens, I. K. Oenig, A. Weller, and D. Fick, *Nucl. Phys. A* **407**, 208 (1983).
- [6] E. F. Aguilera, E. Martínez-Quiroz, D. Lizcano, A. Gómez-Camacho, J. J. Kolata, L. O. Lamm, V. Guimarães, R. Lichtenthäler, O. Camargo, F. D. Becchetti *et al.*, *Phys. Rev. C* **79**, 021601(R) (2009).
- [7] E. F. Aguilera, I. Martel, A. M. Sanchez-Benitez, and L. Acosta, *Phys. Rev. C* **83**, 021601(R) (2011).
- [8] J. Lubian, T. Correa, E. F. Aguilera, L. F. Canto, A. Gomez-Camacho, E. M. Quiroz, and P. R. S. Gomes, *Phys. Rev. C* **79**, 064605 (2009).
- [9] V. Scarduelli, E. Crema, V. Guimarães, D. Abriola, A. Arazi, E. deBarbara, O. A. Capurro, M. A. Cardona, J. Gallardo *et al.*, *Phys. Rev. C* **96**, 054610 (2017).
- [10] N. N. Deshmukh, V. Guimarães, E. Crema, D. Abriola, A. Arazi, E. deBarbara, O. A. Capurro, M. A. Cardona, J. Gallardo *et al.*, *Phys. Rev. C* **92**, 054615 (2015).
- [11] L. A. Parks, K. W. Kemper, A. H. Lumpkin, R. I. Cutler, L. H. Harwood, D. Stanley, P. Nagel, and F. Petrovich, *Phys. Lett. B* **70**, 27 (1977).
- [12] L. R. Gasques, A. S. Freitas, L. C. Chamon, J. R. B. Oliveira, N. H. Medina, V. Scarduelli, E. S. Rossi, M. A. G. Alvarez, V. A. B. Zagatto, J. Lubian, G. P. A. Nobre, I. Padron, and B. V. Carlson, *Phys. Rev. C* **97**, 034629 (2018).
- [13] A. Lépine-Szily, R. Lichtenthäler, and V. Guimarães, *Eur. Phys. J. A* **50**, 128 (2014).
- [14] L. C. Chamon, B. V. Carlson, L. R. Gasques, D. Pereira, C. De Conti, M. A. G. Alvarez, M. S. Hussein, M. A. Candido Ribeiro, E. S. Rossi Jr., and C. P. Silva, *Phys. Rev. C* **66**, 014610 (2002).
- [15] L. F. Canto, P. R. S. Gomes, J. Lubian, M. S. Hussein, and P. Lotti, *Eur. Phys. J. A* **50**, 89 (2014).
- [16] I. J. Thompson, *Comput. Phys. Rep.* **7**, 167 (1988).
- [17] Evaluated Nuclear Structure Data Files, National Nuclear Data Center, Brookhaven National Laboratory, <http://www.nndc.bnl.gov>.
- [18] T. Ohtsubo, Y. Nakayama, T. Izumikawa *et al.*, *Hyperfine Interact.* **88**, 25 (1994).
- [19] L. R. Gasques, L. C. Chamon, P. R. S. Gomes, and J. Lubian, *Nucl. Phys. A* **764**, 135 (2006).
- [20] W. D. M. Rae, <http://www.garsington.eclipse.co.uk>.
- [21] A. G. M. van Hees, A. A. Wolters, and P. W. M. Glaudemans, *Nucl. Phys. A* **476**, 61 (1988); and (private communication).
- [22] L. Coraggio, A. Covello, A. Gargano, and N. Itaco, *Phys. Rev. C* **89**, 024319 (2014).
- [23] W. Richter, M. V. D. Merwe, R. Julies, and B. Brown, *Nucl. Phys. A* **523**, 325 (1991).
- [24] D. M. Brink, *Semi-classical Methods for Nucleus-Nucleus Scattering* (Cambridge University Press, Cambridge, UK, 1985).
- [25] H. Amakawa and K.-I. Kubo, *Nucl. Phys. A* **266**, 521 (1976).
- [26] W. Weiss, P. Egelhof, K. D. Hildenbrand, D. Kassen, M. Makowska-Rzeszutko, D. Fick, H. Ebinghaus, E. Steffens, A. Amakawa, and K. I. Kubo, *Phys. Lett. B* **61**, 237 (1976); and references therein.
- [27] S. Ohkubo, *Phys. Rev. C* **25**, 2498 (1982).
- [28] F. Petrovich, D. Stanley, L. A. Parks, and P. Nagel, *Phys. Rev. C* **17**, 1642 (1978).
- [29] M. B. Golin and S. Kubono, *Phys. Rev. C* **20**, 1347 (1979).
- [30] H. Nishioka, R. C. Johnson, J. A. Tostevin, and K.-I. Kubo, *Phys. Rev. Lett.* **48**, 1795 (1982).